International Journal of Impact Engineering 76 (2015) 139–154

Contents lists available at ScienceDirect

International Journal of Impact Engineering

journal homepage: www.elsevier.com/locate/ijimpeng

# Modeling concrete like materials under sever dynamic pressures

Gabriel Aráoz [a, *], Bibiana Luccioni [a, b]

[a] Structures Institute, National University of Tucumán, Av. Independencia 1800, San Miguel de Tucumán, Argentina
[b] CONICET, Av. Rivadavia 1917, Ciudad de Buenos Aires, Argentina

## ARTICLE INFO

*Article history:*
Received 26 September 2013
Received in revised form
8 September 2014
Accepted 14 September 2014
Available online 28 September 2014

*Keywords:*
Concrete
Constitutive model
Strain rate
Confinement
Compaction

## ABSTRACT

The behavior of concrete, as well as that of all cohesive-frictional materials, is characterized by a strong dependence on hydrostatic pressure and strain rate sensitivity. The stress–strain response is nonlinear and, depending on the loading path, it can show compaction and dilatancy. Due to its internal constitution, the numerical simulation of this type of materials can be done with a great variety of approaches which are mainly differentiated by the modeling scales and the approximation methods used. Appropriate formulation and calibration of the models are necessary to accurately reproduce the physical phenomena involved in the simulated processes.

A general elastic–viscoplastic model for concrete like materials under high strain rate dynamic loads that produce high confinement pressures, like those present in blast actions, is presented in this paper. The model developed is of phenomenological type and it is formulated within the framework of continuum thermodynamics for irreversible processes with internal variables and small strains. Non-associated plastic flow, cap function and hardening functions that depend on the loading path are proposed. The transition between compaction and dilatancy processes observed in triaxial compression experimental tests can be properly reproduced with the non-associated flow consideration and the proposed hardening functions. The cap function allows the appropriate simulation of the material volumetric response for high confinement pressures. The model formulation is general and it can be used for other cohesive-frictional materials.

The numerical integration algorithm is implemented in a 2D finite element dynamic program that allows solving nonlinear problems of solid mechanics in small strains.

For the model validation, static and dynamic tests with different loading paths and confinement levels for many types of concretes and mortars are analyzed. Numerical results are compared with experimental results obtaining a good description of the main characteristics of this type of materials response under high strain rate pressures.

## 1. Introduction

The study of the response of structures under severe loading has received more attention during the last decades due to the great number of accidental and intentional explosion events that have taken place all around the world. The structures behavior under blast and impact loads still presents many challenges due not only to the difficulties in the dynamic action determination but also to the need of the characterization of the dynamic response of the materials [1]. Particularly, the study of concrete behavior under this type of actions represents an important feature for the design and analysis of protective structures, nuclear plants, offshore structures, airports and other constructions of massive use.

Generally and specially in the near field, explosive loads produce the collapse of individual structural members that can be caused by the failure of the material itself due to the effects of the blast wave before the structural response can take place [2–6]. The effects of the pressure wave propagation can also have important consequences in the observed failure modes under impact loads [7,8]. After individual components have failed and depending on the magnitude of the local failure, a progressive structural collapse can be developed [9–11].

Because of the impulsive nature of the actions, the material response is different from that under static or low strain rate loads, presenting a sensible strain rate dependency [12–26]. Moreover, the behavior of concrete like materials, even under static loads, is strongly influenced by the confinement levels [27–35].

Computational mechanics allows the simulation of these problems with different types of approaches like finite differences

---

* Corresponding author.
*E-mail address:* garaoz@herrera.unt.edu.ar (G. Aráoz).

http://dx.doi.org/10.1016/j.ijimpeng.2014.09.009

method, finite elements method [36–41], mesh free techniques [42,43], discrete elements methods [44–47], and combinations of these techniques. In general the criterion for the use of one approach depends on the specific problem to be solved, the material observation scale and the complexity of the phenomena to be described [48]. In this sense, the use of models on a hydrocode platform can represent an attractive tool for the analysis of problems involving complex loads, geometry and boundary conditions [49–51]. In any case, the results obtained from the numerical simulation strongly depend on the constitutive models used for the materials and their ability to reproduce the involved physical phenomena.

A viscoplastic model for concrete like materials under high strain rate and high pressures is developed in this paper. After a brief description of the main characteristics of this type of materials under impulsive loads and the existent constitutive models, the proposed model is described. Finally, the paper is completed with different validation and application examples.

## 2. Behavior of concrete like materials under high strain rate severe pressure

When an explosive load is detonated very close or in contact with a structural member, the pressure peak can reach several GPa in a few milliseconds. Intense shock waves can be generated in the material and they can cause material disintegration. On the other hand, if the explosive load is detonated in the air, shock waves typically reach several hundreds of kPa and decay in 10 ms.

Due to its characteristic heterogeneity, the behavior of concrete is markedly nonlinear, even for low static loads. The typical stress–strain behavior under static uniaxial compression for concretes with different strength (see Table 1) is shown in Fig. 1. It is characterized by a softening range produced by the micro-scale cracking.

In the case of multiaxial quasistatic compression tests, three transitions can be observed in the stress–strain curves. The behavior is elastic up to the first transition point that corresponds to the beginning of the stable crack propagation. Then the nonlinear response develops up to the second transition that corresponds to the beginning of the unstable crack propagation that is coincident with the point of minimum volumetric deformation or maximum compaction. Finally, the last transition is that corresponding to the peak load. Depending on the confinement level, important deformations can be reached (in the order of 15% for axial strains and 12% for the case of volumetric strains). Peak stresses and strains increase with the levels of confinement [27].

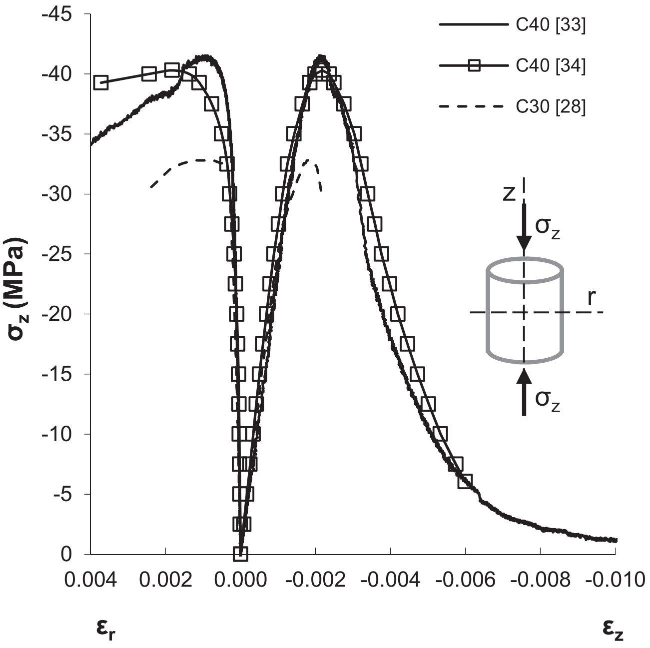

**Fig. 1.** Uniaxial compression tests.

The post-peak response corresponds to strain localization. The greater deformations are localized in cracks vicinity, while the rest of the element unloads exhibiting a decrease of strains.

Many experimental results for concrete [28–35] and mortar [35,52] under static triaxial compression can be found in the literature. As illustration, the results obtained by Vu et al. [33] for C40 concrete are presented in Fig. 2. The results presented by Sfer et al. [28] and Lu et al. [29], like most of the available experimental results, correspond to moderate confinement levels (up to 60 MPa), while experimental results corresponding to high confinement pressures (in the order of 600 MPa) can be found in the papers by Gabet et al. [32], Vu et al. [33] and Poinard et al. [34]. All these authors have observed that dry concrete reaches a limit state characterized by a transition from compaction to dilatancy. This transition can occur for the peak load in the case of low to moderate confinement or during the increment of the axial load in the case of high confinement levels. This behavior is depicted in Fig. 3 where the volumetric response obtained in Vu tests [33] is presented.

**Table 1**
Materials properties of concrete and mortar.

| Material | Concrete | | | | | | | | Mortar | |
|---|---|---|---|---|---|---|---|---|---|---|
| Identification | C40 | C40 | C55 | C40 | C70 | C21 | C30 | C70 | M45 | M46 |
| [Ref] | [33] | [34] | [85] | [86] | [25,88] | [87] | [28] | [89] | [35] | [12] |
| Young modulus, $E$ (MPa) | 24,000 | 26,000 | 31,000 | 20,000 | 39,480 | 19,580 | 26,600 | 30,000 | 20,000 | 20,000 |
| Poisson ratio, $\nu$ | 0.13 | 0.21 | 0.21 | 0.2 | 0.2 | 0.20 | 0.20 | 0.2 | 0.20 | 0.2 |
| Quasistatic compression strength, $f_{c0}$ (MPa) | 41.54 | 40.3 | 56 | 39.3 | 70 | 22.06 | 32.8 | 70 | 45 | 46 |
| Quasistatic compression elastic limit, $f_y$ (MPa) | 32 | 32 | 50 | 32 | 50 | 15 | 24 | 50 | 30 | 34 |
| Compression/tension elastic limit ratio [38], $R_0$ | 10 | 10 | 10 | 10 | 20 | 10 | 10 | 10 | 10 | 10 |
| Biaxial/uniaxial compression strength ratio [38], $R_{bc}$ | 1.16 | 1.16 | 1.16 | 1.16 | 1.16 | 1.16 | 1.16 | 1.16 | 1.16 | 1.16 |
| $\kappa^{vp}$ value for the quasistatic peak compression stress [38] | 0.12 | 0.12 | 0.12 | 0.12 | 0.12 | 0.15 | 0.17 | 0.12 | 0.12 | 0.12 |
| Ratio of octahedral ratios [38], $\gamma$ | 2.2 | 2.2 | 2.2 | 2.2 | 2.1 | 2.2 | 2 | 2.2 | 2.1 | 2.2 |
| Point of confined compression yielding curve [38], $p_h$ (MPa) | 650 | 650 | 650 | 650 | 1000 | 13.79 | 60 | 1000 | 650 | 650 |
| $\sigma_{cu}$ (MPa) | 1600 | 1600 | 1600 | 1600 | 1450 | 80 | 195 | 1450 | 1600 | 1600 |
| Quasistatic tension strength, $f_{t0}$ (MPa) | 4.15 | 4.0 | 5.0 | 6.9 | 3.5 | 2.76 | 2.5 | 7.0 | 4.5 | 3.4 |
| Quasistatic crushing energy, $G_{c0}$ (MPa m) | 1.2E-02 | 1.2E-02 | 1.6E-02 | 1.6E-02 | 1.2E-02 | 6.0E-02 | 1.2E-02 | 1.2E-02 | 1.0E-02 | 1.0E-02 |
| Quasistatic fracture energy, $G_{f0}$ (MPa m) | 1.2E-04 | 1.2E-04 | 1.6E-04 | 1.6E-04 | 1.2E-04 | 3.5E-05 | 1.2E-04 | 1.2E-04 | 1.2E-04 | 1.2E-04 |

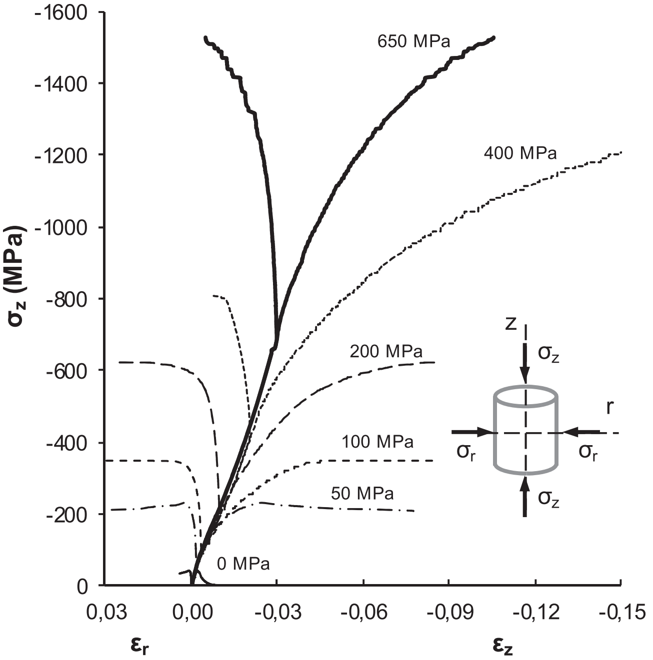

**Fig. 2.** Triaxial compression tests with different confinement levels for C40 concrete by Vu et al. [33].

Another important feature to be noted is the difference in volumetric response of concrete like materials subjected to hydrostatic and oedometric static tests [35].

The behavior under dynamic loads differs from that previously described. In all dynamic events inertial effects appear. On the other side, due to the dynamic nature of the load, certain strain rate is developed in the material while it is deforming. Generally, concrete like materials exhibit rate dependent effects.

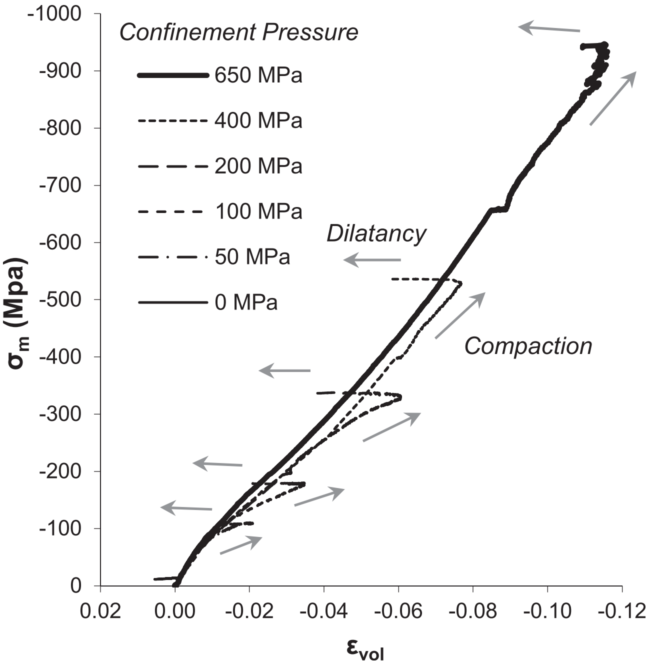

**Fig. 3.** Volumetric behavior in triaxial static compression tests with different confinement levels [33].

The dynamic behavior of concrete is generally experimentally studied using different types of tests. In spite of certain discrepancies related to the strain values corresponding to the maximum stress that can be attributed to the lack of consistency of the testing methods used, an increase in concrete strength under increasing strain rates is always observed [16]. This tendency is observed both in uniaxial compression and uniaxial tension tests but the strain rate sensibility is different for both cases [12–15].

The strength increase under dynamic loads is usually expressed through the dynamic increase factor (DIF) that represents the ratio between the dynamic strength for a given strain rates and the static or quasistatic strength.

Experimental values of the DIF for compression and tension tests [13] are shown in Fig. 4. Dispersion observed can be attributed to the different experimental methodologies used [53], the shape and size of the elements used and the contents and type of aggregates [19,54]. It should be noted that the dynamic amplification is appreciable greater for tension tests and in all cases the dynamic amplification takes place for strain rates at the order of 1–30 s$^{-1}$ [16].

The causes of the strain rate sensitivity are not well established yet. Sercombe et al. [20] consider that the strain rate dependency observed in compression tests is due to the viscous contribution of free water present in material pores. Weerheijm et al. [21] and Ruiz et al. [22], among other authors, state that the DIF observed in tension tests is also due to the viscous effect of water contained in micropores. They observe that not only the tension strength but also the fracture energy are increased with increasing strain rate.

On the other side, recent papers [13,19,23] present other hypothesis for the compression DIF. According to Cotsovos et al. [13] and Schwer [23], the observed DIF is not an actual strength increase but it is exclusively due to the confinement effect produced by the lateral inertia forces. Since concrete like materials are frictional materials, their shear strength is increased with increasing confinement under increasing strain rates. Hao et al. [19] suggest that the strain rate effect depends not only on the specimen dimensions but also on its shape and the aggregates used for the concrete. Other authors have also studied the effect of aggregates in tension [54] and compression DIF [26]. Hao et al. [19] consider that the DIF is a result of a combination of lateral inertial confinement

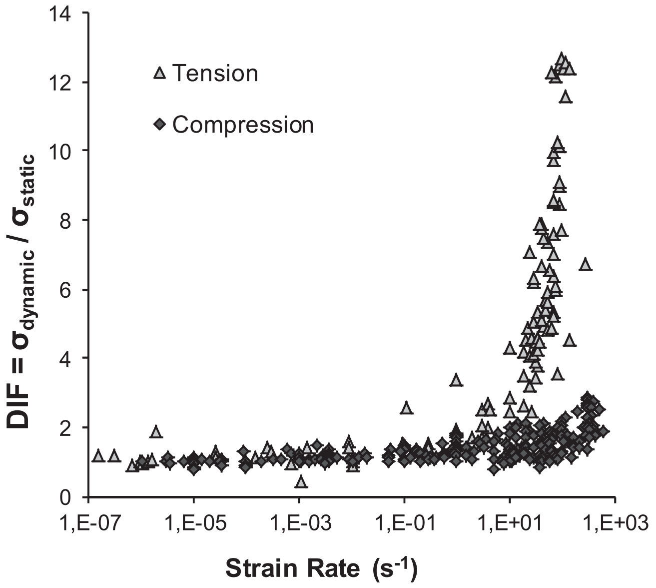

**Fig. 4.** DIF. Experimental results for compression and tension tests [13].

and material viscous effects. Mu et al. [55], state that the apparent DIF under low strain rates is due to the friction effects on proves ends, while the DIF observed for high strain rates is mainly due to lateral inertial confinement.

There are also other material properties affected by the strain rate like the Young modulus and the deformation energy [14,22,24,37].

There is very little experimental information about triaxial tests under high strain rates. The experimental results obtained by Forquin et al. [25] from oedometric tests of C70 concrete (see Table 1) under different strain rates (80, 141 and 221 $s^{-1}$) are presented in Fig. 5. These results show that for the strain rate range analyzed, the deviatoric response does not depend on the strain rate up to a hydrostatic pressure of 500 MPa. For greater confinement pressure the maximum deviator stress is greater than that obtained in static triaxial tests. Strain rate seems to have no effect on dynamical volumetric response but when compared with static response an increase of bulk modulus due to strain rate is observed.

## 3. Concrete models. Brief review

The numerical implementation of constitutive models capable of reproducing the most important characteristic of the material response described in previous section is required for the computer simulation of concrete structures under impulsive loads. Although the physical mechanisms responsible for the strain rate dependency are not yet well established, if there is any material effect it is important to properly incorporate it in the constitutive models formulation [56]. Moreover, the analysis of local effects and the material rupture require great fidelity of numerical models with a proper description of material and numerical algorithms that allow reproducing problems with high strain rates and the development of discontinuities.

The classification of existent constitutive models can be based on different criteria. Some of these criteria are related to the level at which the model is generated and the type of mathematical theory used for the model development. Both of them define the model capacity to simulate the different phenomena experimentally observed. Additionally, the scale at which the model is generated conditions the type of numerical approximation that can be used for the numerical simulation of the problem. On the other side, there are some models differences according to the numerical approximation method used for the solution of the structural problem. These differences are actually imposed by the need of adapting the models to the corresponding numerical tool but they also give possibilities of reproducing phenomenological aspects of the problem more or less rigorously.

In most practical applications concrete is generally considered as a homogeneous material with macro or phenomenological models that establish tensor stress–strain relations to describe the observed behavior resulting from subjacent phenomena related to the internal constitution of the material that this type of model actually do not take into account. As a consequence, this type of models can only implicitly describe complex phenomena due to the internal structure through internal variables associated to them. Moreover, due to the general complexity, the determination of the parameters taking place plays an important role in the models behavior.

Macroscopic models include many different models. Generally these models can be classified in rate independent and rate dependent methods. Among rate independent models there are models based on nonlinear elasticity [57], smeared crack models [58], plasticity models [59], damage models [60] or combination of these types of models [36,38]. Viscoelastic models [39], viscoplastic models [61], viscous damage [37] or combination of them [40,41] are generally used to model rate dependent concrete behavior.

The response of concrete under high strain rates involves stress waves drastically varying in space and time. The band width off the stress wave is comparable with the size of the mesoscopic heterogeneities (nominal aggregates size) [62]. This fact explains the potential effects of heterogeneities on the response under this type of actions and justifies the advantages of meso-scale modeling of concrete in the detailed description of the mechanical processes taking place in the material. Meso-models consider material heterogeneities through the definition of different zones with continuous properties and the global response of the material is obtained with some kind of homogenization technique. Nevertheless, the great computational demand associated to meso-scale modeling can make the use of this type of models prohibited for the solution of practical problems.

Different authors have used meso-scale models for the description of concrete behavior like a composite material

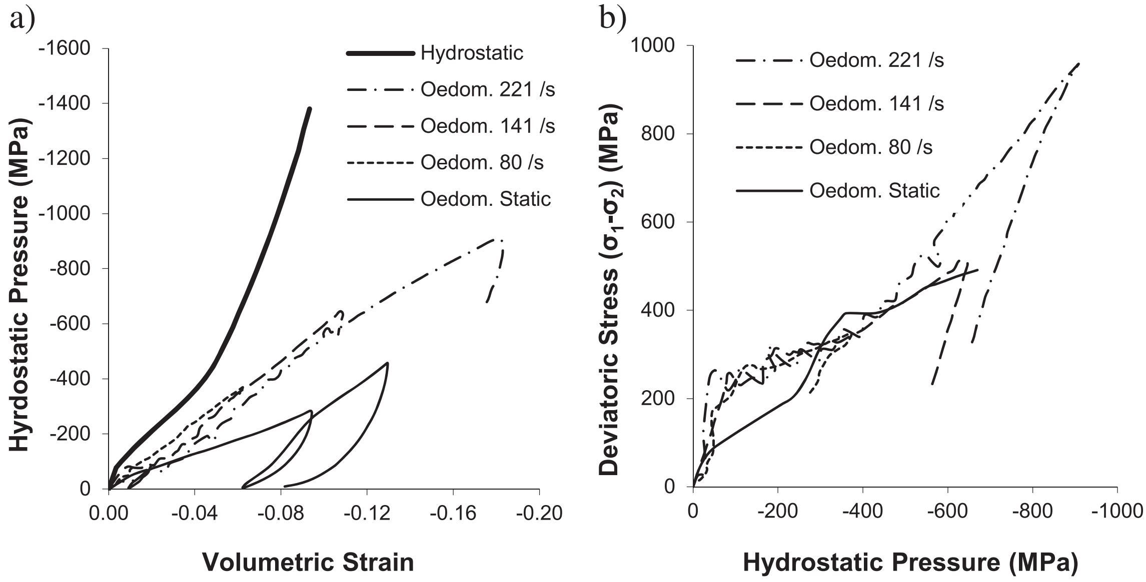

**Fig. 5.** Experimental results obtained from dynamic oedometric tests under different strain rates [25]. a) Hydrostatic pressure vs volumetric strain for different tests; b) Load path for different tests.

[26,27,49,51,63]. Micro-plane models [64] and particle methods [42,43] are also some particular types of mesoscopic models used for concrete.

Finally, micromechanical models allow the study of heterogeneous materials through homogenization procedures [65,66]. At this scale non hydrated cement grains, calcium hydroxide particulates and the concrete porous structure can be identified. An alternative to micro-scale modeling are discrete element methods [47] that represent powerful tools for the simulation of granular material, particle systems and also solids, especially those that change from a continuous to a discontinuous medium. This type of methods normally represents the continuous medium as a set of discrete elements interacting according to certain contact laws.

### 3.1. Analysis of existing models

Simulation of very complex situations including blast phenomena and fluid-structure interaction is nowadays possible using hydrocodes that are explicit dynamic codes particularly suitable for reproducing highly nonlinear structures response under impulsive loads. Tu and Lu [50] present a detailed revision of concrete models used in commercial hydrocodes. These models share some common characteristics. Volumetric and deviatoric parts of constitutive laws are split. The volumetric response is governed by the equation of state (EoS) that relates the hydrostatic pressure with specific volume and energy or temperature. Some of the equations of state suitable for brittle porous materials like concrete are: pice-wise linear EoS, compaction EoS and p-alpha EoS. All these EoS are based on Mie–Gruneisen EoS. Deviatoric part is obtained with the strength model that normally involves the definition of yield surfaces. Most available strength models for concrete are plastic damage models. Some of them are briefly described in what follows.

JH2 [50,67] model for concrete is linear elastic up to a certain yield criterion from which plastic strains begin to develop. Damage is accumulated until failure and then a residual state is presented by the material. An initial failure surface, a post failure surface and a fracture surface are defined. The post failure surface is obtained scaling the failure surface with the damage index that depends on the pressure dependent fracture strain and the incremental equivalent plastic strain, including deviatoric and volumetric plastic strain. In this way, the cohesion loss contributing to global damage during the compaction process can be represented. The independence of the third stress invariant implies a limitation to adequately represent stress states in octahedral planes. A single cut-off value is used to limit fracture strain. On the other side, strain rate effect is modeled amplifying the strength surface for a fix pressure value. The amplification factor is identical for tension and compression.

K&C model was developed by Malvar et al. [68,69] and has been improved more recently [70]. Three independent strength surfaces are defined in K&C model: the initial yield surface, the failure surface and the residual surface. Three stress invariants (I1, J2 and J3) are involved in these surfaces definitions that present curve meridians. Loading surfaces after initial yield and post failure surfaces are obtained by interpolation between the respective surfaces. Nonlinear behavior is controlled by a damage function that takes different forms in tension and compression and depends on the effective plastic strain. The failure surface depends on the strain rate through dynamic amplification factors that are different for tension and compression.

The GR model [71] is an extension of JH model with various improvements and additions such as the inclusion of the third stress invariant in loading surface definition. Moreover, the yielding surface is smooth along all the pressure range. The increment of strength with strain rate is reformulated to take into account material damage. The global damage is composed of the damage due to the volumetric compaction and calculated as a function of total volumetric strain and damage due to plastic strain deviation calculated as a function of the effective plastic strain like in JH model.

RHT model [72] is also an improvement of JH model including new features like strain hardening, dependence of the third stress invariant, consideration of a residual surface and strain rate dependence of hydrostatic tension strength. The shape of the yielding surface on the octahedral planes is an improvement of that of K&C model with the addition of an octahedral ratios ratio that varies with hydrostatic pressure. The initial yielding surface includes a cap function producing yielding surface closure on the hydrostatic axis for high confining pressures. Both the initial yielding surface and the residual surface that is independent of the third stress invariant are obtained scaling the failure surface as a function of the damage index that is independent of volumetric plastic strain like in JH model. Strain rate dependence is taken into account through a dynamic amplification factor affecting hydrostatic tension strength (yielding surface shift) and deviatoric strength (yielding surface amplification). Dynamic amplification is overestimated in this model and this fact can cause a problem in numerical simulation of high strain rate dynamic problems. Tu and Lu [73] presented some improvements to RHT model: dependence of the failure surface on the third stress invariant, octahedral ratios ratio dependence on the hydrostatic pressure, tension dynamic amplification factor improvement and consideration of a bilinear strain softening based on fracture energy concept.

HPG model [74] combines various existent approaches. The static failure surface is based on the known values of compression, tension and shear strength. Meridians are curve and a piecewise function is used for low pressure values. The shape of the failure surface on the deviatoric plane is similar to that presented by Willam and Warnke [75]. Strain rate dependence is taken into account through a radial amplification of the yielding surface with dynamic amplification factors (DIF) [68]. New expression for the DIF is proposed to better reproduce experimental results. Due to plastic strain hardening, the initial yielding surface grows until it reaches the failure surface and then, damage and strain softening take place. During strain hardening, associated flaw is used for low pressures while von Mises flaw is used for high pressures. Shear and compaction damage are distinguished in HPG model. Shear damage is based on JH model [67] model while compaction damage follows Ruppert's proposal [71].

All the described models are macro models. Zhou and Hao [76] present a meso-scale heterogeneous model for concrete material under blast loading. Concrete is assumed as a two phases composite formed by a cement paste matrix with aggregate inclusions. Perfect bond between aggregates and cement paste is assumed but some models also include an interfacial transition zone (ITZ) [77]. Piecewise-linear porous EoS with tensile failure defined by a minimum pressure limit is used for mortar. Mortar strength behavior is modeled with a piece-wise Drucker–Prager model. Damage is obtained combining tension and compression damage scalars that are functions of the equivalent tensile and compressive strains. Compressive and tensile strength surface is amplified using compressive and tensile DIF respectively. Linear EoS and the same strength model used for mortar but with different parameters are used for the aggregates. DIF is also used for aggregates.

In contrast with the above models, there are a few models developed to model concrete dynamic behavior in finite element codes that do not decouple spherical and deviatoric response and are capable of reproducing concrete behavior under moderate or high hydrostatic pressure [35,38,78]. Most of these models are based on plasticity and/or damage theories and thus, they are rate independent and cannot reproduce concrete behavior under high strain rate. There are other models based on viscoplasticity and/or viscous damage that take into account strain rate dependence and history effects [37] but they cannot reproduce concrete behavior under high confining pressures.

The analysis of available models shows that most of them are not able to simultaneously and properly consider the main effects of impulsive loads described in Section 2: effect of high confinement pressures, transition from compaction to dilatancy and material dynamic strength amplification.

## 4. Proposed model

### 4.1. Introduction

The proposed model consists of an improvement and an extension of the model by Luccioni and Rougier [38] in order to better describe concrete like materials behavior under impulsive loads. This type of actions is characterized by dynamic high confinement pressures resulting in dynamic strength amplification and transition from compaction to dilatancy under compression.

The model is a phenomenological model formulated in the frame of continuum mechanics considering small strains. Elastic properties degradation under high confinement pressures is neglected [34]. The model is derived from a Perzyna [61] viscoplastic extension of an improved generalized plastic model.

The main difference between the proposed model and models normally used in hydrocodes [50,67–77] is that volumetric and deviatoric response are jointly considered. Like in most of those models, a yield surface that evolves from an initial yield surface to a maximum loading surface or failure surface and finally reduces following strain softening is considered. In coincidence with some of those models, this surface closes on the hydrostatic axis. Instead of using one or two damage parameters to scale the loading surface, the evolution of the loading surface is implicitly controlled by two internal variables related to viscoplastic work and viscoplastic volumetric strain differentiating tension and compression stress states. In this way, the effect of loading history on inelastic response can be reproduced. The definition of a plastic potential function that evolves with the internal variables allows simulating transition from compaction to dilatancy under high confining pressures. Moreover, the effect of strain rate dependence is naturally obtained from viscoplasticity theory and implicitly leads to dynamic amplification of strength depending on the strain rate history not only on the actual strain rate like in inviscid models in which a DIF is introduced to take into account strain rate dependence.

Compared with other existing viscoplastic models, the definitions of the yielding surface, internal variables, hardening/softening laws and flaw laws in the model presented in this paper make them more suitable for reproducing concrete like materials mechanical behavior under high confining static or dynamic loads.

### 4.2. Thermodynamic basis

The model is based on the assumption of uncoupled elasticity [79] according to which the free Helmholtz energy per volume unit $\psi$ can be supposed to be formed by two independent parts: an elastic part $\psi^e$ and a viscoplastic part $\psi^{\mathrm{vp}}$ corresponding to the elastic and viscoplastic processes respectively

$$\psi\left(\varepsilon^e_{ij}, \alpha^{\mathrm{vp}}_i\right) = \psi^e\left(\varepsilon^e_{ij}\right) + \psi^{\mathrm{vp}}\left(\alpha^{\mathrm{vp}}_i\right) \tag{1}$$

where $\varepsilon^e_{ij}$ is the elastic strain tensor and $\alpha^{\mathrm{vp}}_i$ represents a set of viscoplastic internal variables that will be defined later.

For small strains the elastic part of the free energy density can be written as a quadratic expression of the elastic strain tensor,

$$\psi^e\left(\varepsilon^e_{ij}\right) = \frac{1}{2}\left(\varepsilon^e_{ij}C_{ijkl}\varepsilon^e_{kl}\right) \tag{2}$$

where $C_{ijkl}$ is the elastic constitutive tensor.

The plastic model in which the proposed model is based [38] includes only one internal variable, the plastic hardening variable $\kappa^p$. It can be shown that the non-isotropic plastic hardening exhibited by concrete like materials under non proportional load histories reaching high hydrostatic pressures cannot be properly described using only one internal viscoplastic variable based on viscoplastic work that does not distinguish between volumetric and deviatoric behavior. For this reason, the proposed model includes a new internal variable, the volumetric viscoplastic variable. The viscoplastic part of the free energy density is written as,

$$\psi^{\mathrm{vp}}(\alpha_i) = \psi^{\mathrm{vp}}\left(\kappa^{\mathrm{vp}}, \kappa^{\mathrm{vp}}_v\right) \tag{3}$$

where $\kappa^{\mathrm{vp}}$ is the viscoplastic damage variable and $\kappa^{\mathrm{vp}}_v$ is the volumetric viscoplastic variable.

Clausius–Duhem inequality can be written as,

$$\Xi = -\dot{\psi} - \eta\dot{\theta} + \sigma_{ij}\,\dot{\varepsilon}_{ij} - \frac{1}{\theta}q_i\theta_i \geq 0 \tag{4}$$

where $\Xi$ is the dissipation density per unit volume, $\theta$ is a temperature measure, $\eta$ is the entropy density per unit volume and $q_i$ the heat flux through external surface.

Assuming an additive strain decomposition

$$\dot{\varepsilon}_{ij} = \dot{\varepsilon}^e_{ij} + \dot{\varepsilon}^{\mathrm{vp}}_{ij} \tag{5}$$

in an elastic part $\dot{\varepsilon}^e_{ij}$ and a viscoplastic part $\dot{\varepsilon}^{\mathrm{vp}}_{ij}$ and taking into account equations (1) and (2) it results,

$$\begin{aligned}\Xi = {} & \left(\sigma_{ij} - \frac{\partial\psi^e}{\partial\varepsilon^e_{ij}}\right)\dot{\varepsilon}^e_{ij} - \left(\frac{\partial\psi}{\partial\theta} + \eta\right)\dot{\theta} + \sigma_{ij}\dot{\varepsilon}^{\mathrm{vp}}_{ij} - \frac{\partial\psi^{\mathrm{vp}}}{\partial\kappa^{\mathrm{vp}}}\dot{\kappa}^{\mathrm{vp}} \\ & -\frac{\partial\psi^{\mathrm{vp}}}{\partial\kappa^{\mathrm{vp}}_v}\dot{\kappa}^{\mathrm{vp}}_v - \frac{1}{\theta}q_i\nabla\theta \geq 0\end{aligned} \tag{6}$$

As $\dot{\varepsilon}^e_{ij}$ and $\dot{\theta}$ represent arbitrary temporal variations of free variables, sufficient conditions to fulfill Clausius–Duhem inequality are provided by,

$$\begin{aligned}& \sigma_{ij} - \frac{\partial\psi^e}{\partial\varepsilon^e_{ij}} = 0 \Rightarrow \sigma_{ij} = \frac{\partial\psi^e}{\partial\varepsilon^e_{ij}} = C_{ijkl}\varepsilon^e_{kl} = C_{ijkl}\left(\varepsilon_{kl} - \varepsilon^{\mathrm{vp}}_{kl}\right) \\ & \frac{\partial\psi}{\partial\theta} + \eta = 0 \Rightarrow \eta = -\frac{\partial\psi}{\partial\theta}\end{aligned} \tag{7}$$

where $\varepsilon_{ij}$ represents the total strain tensor.

Additionally, for uncoupled thermo-mechanical problems, mechanical dissipation should fulfill the first Clausius–Planck inequality,

$$\Xi^{\mathrm{vp}}_m = \sigma_{ij}\dot{\varepsilon}^{\mathrm{vp}}_{ij} - \frac{\partial\psi^{\mathrm{vp}}}{\partial\kappa^{\mathrm{vp}}}\dot{\kappa}^{\mathrm{vp}} - \frac{\partial\psi^{\mathrm{vp}}}{\partial\kappa^{\mathrm{vp}}_v}\dot{\kappa}^{\mathrm{vp}}_v \geq 0 \tag{8}$$

### 4.3. Yield function

A yield function $F$ is defined to limit elastic range so that the behavior is elastic for $F < 0$ and viscoplastic for $F \geq 0$.

For both static and dynamic loads, the response of concrete is markedly influenced by the confinement level. As general rule, the strength increases with the hydrostatic pressure but the variation is not linear, especially for high confinement levels. Moreover, plastic compaction can take place under hydrostatic states of stress. For these reasons, a yielding function with curve meridians and intersecting the hydrostatic axis is proposed in this paper [80]. The yield function is defined as follows,

$$F\left(\sigma_{ij};\kappa^{\mathrm{vp}},\kappa_v^{\mathrm{vp}}\right)=\sqrt{3J_2}+\quad F_{\mathrm{cap}}\left(I_1,\kappa_v^{\mathrm{vp}}\right)\left[\alpha I_1+\beta\langle\sigma_{\max}\rangle-\gamma\langle-\sigma_{\max}\rangle+\frac{\delta(1-\alpha)}{K\left(\sigma_{ij},\kappa^{\mathrm{vp}},\kappa_v^{\mathrm{vp}}\right)}I_1^2-K\left(\sigma_{ij},\kappa^{\mathrm{vp}},\kappa_v^{\mathrm{vp}}\right)(1-\alpha)(1+\delta)\right]=0 \tag{9}$$

where $\alpha$, $\beta$, $\gamma$ and $\delta$ are material parameters that control the shape of the yield function. $I_1$ is the first invariant of the stress tensor, $J_2$ is the second invariant of the deviator stress tensor, $K(\sigma_{ij},\kappa^{\mathrm{vp}},\kappa_v^{\mathrm{vp}})$ represents the evolution of the equivalent yielding threshold, $\sigma_{\max}$ is the maximum principal stress: $\sigma_3\leq\sigma_2\leq\sigma_1=\sigma_{\max}$.

Parameters $\alpha$, $\beta$, $\gamma$ and $\delta$ are obtained in the same way described in Ref. [38].

The function $F_{\mathrm{cap}}$ that depends on the volumetric viscoplastic variable $\kappa_v^{\mathrm{vp}}$, allows the closure of the yield function on the hydrostatic axis. The following expression plotted in Fig. 6 is proposed,

$$F_{\mathrm{cap}}\left(I_1,\kappa_v^{\mathrm{vp}}\right)=\begin{cases}1 & I_1\geq I_u\left(\kappa_v^{\mathrm{vp}}\right)\\ 1-\left(\dfrac{I_u\left(\kappa_v^{\mathrm{vp}}\right)-I_1}{I_0\left(\kappa_v^{\mathrm{vp}}\right)-I_u\left(\kappa_v^{\mathrm{vp}}\right)}\right)^2 & I_1<I_u\left(\kappa_v^{\mathrm{vp}}\right)\end{cases} \tag{10}$$

$I_0(\kappa_v^{\mathrm{vp}})$ corresponds to the value of $I_1$ for which the yield surface intersects the hydrostatic axis and $I_u(\kappa_v^{\mathrm{vp}})$ is the value of $I_1$ for which the yield curve in the compression meridian departs from the curve in the original model [38].

The effect of function $F_{\mathrm{cap}}$ on the yield function is sketched in Fig. 7. The use of this function makes possible a better reproduction of experimental results for high confinement pressures. The yield function evolves with the hardening process depending on the loading path and can reach the failure surface. The failure surface is sketched in Fig. 8 together with the initial yield surface. Since $F_{\mathrm{cap}}=1$ for failure, the failure surface is coincident with that used in Ref. [38].

In order to properly represent the response of concrete under high confinement triaxial pressures, the proposed model considers that function $F_{\mathrm{cap}}$ depends on a new internal variable related to the viscoplastic compaction process, the volumetric viscoplastic variable, $\kappa_v^{\mathrm{vp}}$.

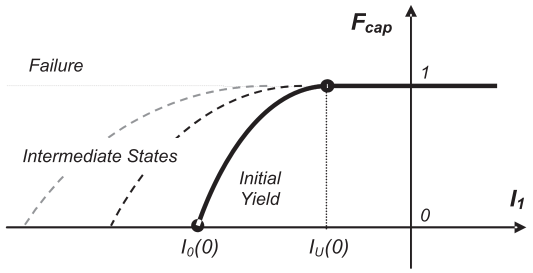

**Fig. 6.** $F_{\mathrm{cap}}$ function.

Function $F_{\mathrm{cap}}$ only produces a progressive closure of the yield surface on the hydrostatic axis without modifying the shape of the original yield curve [38] on the deviatoric planes. Unlike other models, see for example [72], the shape of the yield curve on the deviatoric planes does not depend on the hydrostatic pressure. This simplification does not represent a limitation when loading paths lying on the compressive meridian plane are analyzed but the model should be improved to properly represent stress paths including tension.

### 4.4. Viscoplastic flow

The following flow rule is used for viscoplastic strains,

$$\dot{\varepsilon}_{ij}^{\mathrm{vp}}=\frac{\phi\left[F\left(\sigma_{ij};\kappa^{\mathrm{vp}},\kappa_v^{\mathrm{vp}}\right)\right]}{\eta}\frac{\partial G\left(\sigma_{mn};\kappa^{\mathrm{vp}},\kappa_v^{\mathrm{vp}}\right)}{\partial\sigma_{ij}} \tag{11}$$

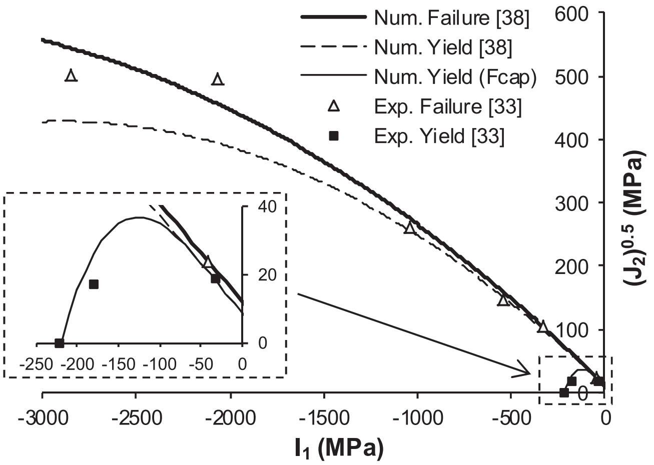

**Fig. 7.** Modified yield surface. Comparison with experimental results [33] for C-40 concrete.

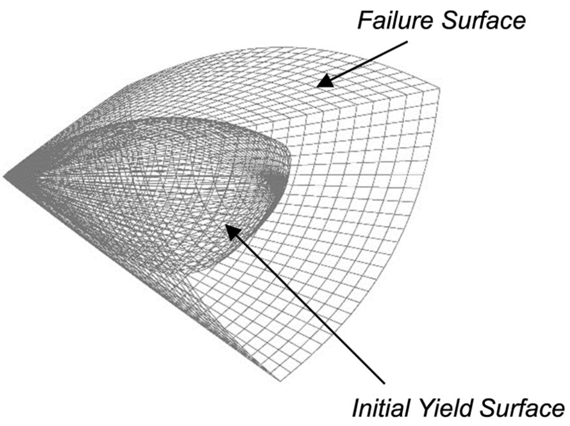

**Fig. 8.** Failure surface and initial yield surface.

where $\eta$ is the viscosity parameter, $G(\sigma_{mn},\kappa^{\mathrm{vp}},\kappa_v^{\mathrm{vp}})$ is the plastic potential surface and $\phi[F(\sigma_{ij},\kappa^{\mathrm{vp}},\kappa_v^{\mathrm{vp}})]$ is the overstress function defined as,

$$\phi\left[F\left(\sigma_{ij};\kappa^{\mathrm{vp}},\kappa_v^{\mathrm{vp}}\right)\right]=\left\langle F\left(\sigma_{ij};\kappa^{\mathrm{vp}},\kappa_v^{\mathrm{vp}}\right)\right\rangle^N \tag{12}$$

where the symbols $\langle\rangle$ represent the Macaulay brackets $\langle x\rangle = 0.5(x+|x|)$;

The exponent $N$ and the viscosity coefficient $\eta$ are material parameters that depend on the type of stress state (tension or compression) and must be obtained from tension and compression tests with different strain rates.

The magnitude order of the viscosity coefficient can be estimated through the following expression [81]:

$$\eta_c=\frac{l\sqrt{E\rho}}{2f_y} \tag{13}$$

where $l$ is the characteristic length used in the model generally depending on the maximum aggregates size; $E$ is the Young modulus, $\rho$ is the density and $f_y$ the elastic limit stress.

represent the behavior described in Section 2 a new internal variable, $\kappa_v^{\mathrm{vp}}$, is included in the model to independently control the cap evolution given by function $F_{\mathrm{cap}}$. Both internal variables are related to inelastic strains but can vary in different ways depending on the viscoplastic process evolution. In this way, the effect of inelastic deviatoric and volumetric strains is indirectly taken into account.

The isotropic hardening variable, called viscoplastic damage variable $\kappa^{\mathrm{vp}}$ is obtained normalizing viscoplastic work to unity. It varies from 0 for the virgin material to 1 when all energy that the material is able to dissipate has been consumed. The following evolution rule that takes into account the differentiated behavior in tension and compression is used [38,83],

$$\dot{\kappa}^{\mathrm{vp}}=\underbrace{\left[\frac{r}{g_f^{*\mathrm{vp}}}+\frac{(1-r)}{g_c^{*\mathrm{vp}}}\right]\sigma_{ij}}_{H_{ij}}\ \dot{\varepsilon}_{ij}^{\mathrm{vp}} \tag{16}$$

$$\begin{gathered}
g_f^{*\mathrm{vp}}=\left(\frac{\sum_{i=1}^{3}|\sigma_i|R^{\mathrm{ovp}}}{f^{\mathrm{vp}}\left[F_{\mathrm{cap}}\left(I_1,\kappa_v^{\mathrm{vp}}\right)\right]^2}\right)^{1+\mathrm{J}(-\mathrm{r})} g_f^{\mathrm{vp}}\quad g_c^{*\mathrm{vp}}=\left(\frac{\sum_{i=1}^{3}|\sigma_i|}{f^{\mathrm{vp}}\left[F_{\mathrm{cap}}\left(I_1,\kappa_v^{\mathrm{vp}}\right)\right]^2}\right)^{1+\mathrm{J}(-\mathrm{r})} g_c^{\mathrm{vp}}\\
J\left(-r\right)=\begin{cases}0 & r>0\\ 1 & r\leq 0\end{cases}\\
f^{\mathrm{vp}}=\frac{1}{(1-\alpha)(1+\delta)}\left[\frac{\sqrt{3J_2}}{F_{\mathrm{cap}}\left(I_1,\kappa_v^{vp}\right)}+\alpha I_1+\beta\langle\sigma_{\max}\rangle-\gamma\langle-\sigma_{\max}\rangle+\frac{\delta(1-\alpha)}{K\left(\sigma_{ij},\kappa^{\mathrm{vp}},\kappa_v^{\mathrm{vp}}\right)}I_1^2\right]
\end{gathered} \tag{17}$$

General expressions are proposed in this paper for the viscoplastic parameters corresponding to different stress combinations.

$$\begin{aligned}\eta&=r\eta_t+(1-r)\eta_c\\ N&=rN_t+(1-r)N_c\end{aligned} \tag{14}$$

where ($\eta_t$ and $N_t$) and ($\eta_c$ and $N_c$) are the parameters corresponding to uniaxial tension and compression respectively and

$$r=\frac{\sum_{i=1}^{3}\langle\sigma_i\rangle}{\sum_{i=1}^{3}|\sigma_i|} \tag{15}$$

with $\sigma_i$ representing the principal stresses.

As a particular case Eq. (12) corresponds to the inviscid case when $\eta\to 0$. It should be taken into account that from the numerical point of view, as $\eta\to 0$ the problem becomes ill conditioned. This fact is the origin of difficulties in the calculus process that have motivated the development of different integration algorithms that obtain the rate dependent solution as a function of the inviscid solution [82].

### 4.5. Internal variables

The description of the yield surface change of size can be done with only one isotropic hardening variable $\kappa^{\mathrm{vp}}$ depending on the inelastic strains through a scalar measure of them. Nevertheless, to

$R^{\mathrm{ovp}}$ is the ratio between the compression and tension yield thresholds, $g_f^{\mathrm{vp}}$ and $g_c^{\mathrm{vp}}$ are the values of the maximum energy dissipated in uniaxial tension and compression processes respectively. They are evaluated as follows,

$$g_f^{\mathrm{vp}}=\frac{G_f}{l_c}\quad\text{and}\quad g_c^{\mathrm{vp}}=\frac{G_c}{l_c} \tag{18}$$

where $G_f$ and $G_c$ are the fracture and crushing energy values and $l_c$ is an external parameter (characteristic length) that depends on the characteristic size of the finite element mesh that is included in the model to preserve response objectivity with respect to the mesh size.

Many experimental works showing the dependence of strain energy on the strain rate can be found [14]. From these experimental results different analytical expressions have been proposed. The expressions presented in Ref. [84] are used in this paper. They are derived from those proposed by Luege [37] and Ngo et al. [18], which have been modified to take into account the available experimental results.

The evolution of the volumetric viscoplastic variable $\kappa_v^{\mathrm{vp}}$ is defined as,

$$\dot{\kappa}_v^{\mathrm{vp}}=\langle-\dot{\varepsilon}_{ii}^{\mathrm{vp}}\rangle \tag{19}$$

where

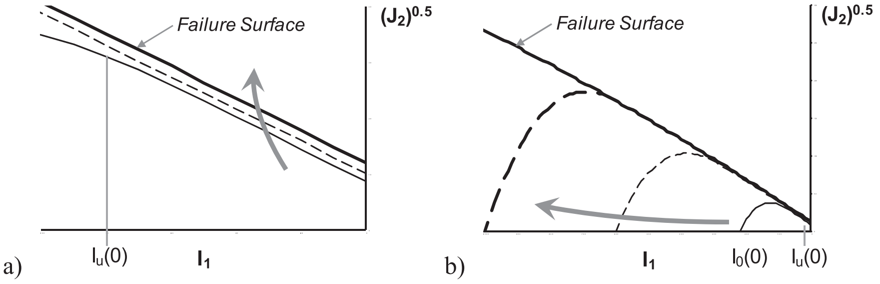

**Fig. 9.** Schematic evolution of the yield surface for different loading paths: a) Low and moderate confinement; b) High confinement.

$$\langle -\dot{\varepsilon}_{ii}^{\mathrm{vp}}\rangle = \frac{1}{2}\left(-\dot{\varepsilon}_{ii}^{\mathrm{vp}} + \left|\dot{\varepsilon}_{ii}^{\mathrm{vp}}\right|\right) \tag{20}$$

The symbol $\langle -\dot{\varepsilon}_{ii}^{\mathrm{vp}}\rangle$ is used to account only for compaction viscoplastic strains.

### 4.6. Plastic hardening

The numerical simulation of concrete like material behavior under high confinement pressures requires the proper definition of the yielding function evolution. The hardening processes for different loading paths are schematically represented in Fig. 9.

The yield surface evolution, controlled by $\kappa^{\mathrm{vp}}$, represents a change of size in deviatoric and hydrostatic directions (Fig. 9a). This type of hardening is prevailing for deviatoric stress states or low confinement states in which volumetric viscoplastic strain is not negative (dilatancy).

A plastic compaction that produces the evolution of the function $F_{\mathrm{cap}}$ takes place under compression with high confinement pressures (Fig. 9b). The intersection of the yield surface with the deviatoric plane is gradually closing with increasing hydrostatic pressure.

The volumetric viscoplastic variable $\kappa_v^{\mathrm{vp}}$ controls de evolution of $F_{\mathrm{cap}}$ and this is the main cause of hardening for high confinement pressures.

The following evolution, that constitutes an extension of that in the previous model [38] is proposed in this paper for the plastic hardening due to $\kappa^{\mathrm{vp}}$,

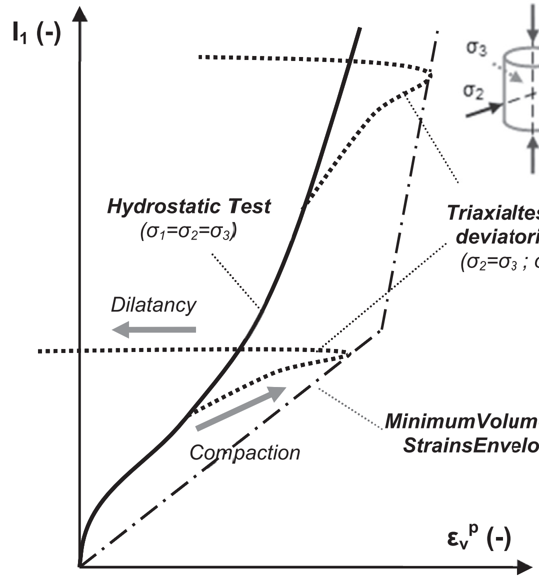

**Fig. 10.** Triaxial test sketch. Compaction-dilatancy transition.

$$K\left(\sigma_{ij}, \kappa^{\mathrm{vp}}, \kappa_v^{\mathrm{vp}}\right) = \left[r\sigma_t\left(\kappa^{\mathrm{vp}}\right) + (1-r)\sigma_c\left(\kappa^{\mathrm{vp}}\right)\right]F_{\mathrm{cap}}\left(I_1, \kappa_v^{\mathrm{vp}}\right) \tag{21}$$

where $\sigma_{\mathrm{t}}(\kappa^{\mathrm{vp}})$ and $\sigma_c(\kappa^{\mathrm{vp}})$ represent the evolution of yielding thresholds in static uniaxial tension and compression respectively.

The hardening due to the evolution of the cap is controlled by the functions $I_0(\kappa_v^{\mathrm{vp}})$ and $I_u(\kappa_v^{\mathrm{vp}})$ that should be properly defined during compaction and dilatancy.

The response of cohesive-frictional material in a triaxial test is sketched in Fig. 10. First a hydrostatic pressure is applied and then, axial compression is incremented producing a deviatoric stress state. During the deviatoric process, compaction takes place up to a certain point from which the dilatancy process begins. This point corresponds to the envelope of minimum volumetric strains and can be obtained from experimental results.

The transition from plastic compaction to plastic dilatancy is defined when the viscoplastic volumetric variable reaches the minimum volumetric strains envelope. The few experimental results available [32] show that this envelope curve approximately matches the curve obtained with an oedometric test.

The evolution rules for $I_0$ and $I_u$ during the compaction process are obtained from the experimental results of a hydrostatic compression test. $I_0(\kappa_v^{\mathrm{vp}})$ represents the evolution of the first stress invariant ($I_1 = 3\,p = \sigma_1 + \sigma_2 + \sigma_3$) as a function of the volumetric viscoplastic volumetric strain in a static hydrostatic compression test. The following rule is proposed to generalize this evolution to other stress paths,

$$I_0\left(\kappa_v^{\mathrm{vp}}\right) = I_0^{\mathrm{Hydro}}\left(\widehat{\kappa}_v^{\mathrm{vp}}\right) \text{with } \widehat{\kappa}_v^{\mathrm{vp}} = \frac{\kappa_v^{\mathrm{vp}}}{4 - n_n} \tag{22}$$

where $n_n$ represents the number of non-null strain components.

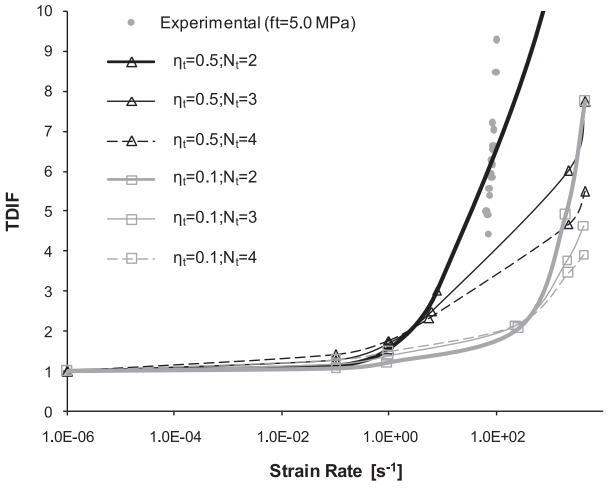

**Fig. 11.** TDIF. Tension viscoplastic parameters calibration. Experimental results by Brara and Klepaczko [85].

The variation of $I_u(\kappa_v^{\text{vp}})$ should be given to complete the definition of function $F_{\text{cap}}$. It should be observed that while in an oedometric test the material yields very soon and $I_u(\kappa_v^{\text{vp}})$ remains fix and equal to its initial value $I_u(0)$, in other cases it varies allowing a gradual increase of the yield surface with the increase of deviatoric stresses, during the compaction process. The following expression is proposed to define the evolution of $I_u(\kappa_v^{\text{vp}})$

$$I_u(\kappa_v^{\text{vp}}) = I_0^{\text{Hydro}}(\tilde{\kappa}_v^{\text{vp}}) \text{ with } \tilde{\kappa}_v^{\text{vp}} = \kappa_v^{\text{vp}}\left(\frac{n_n - 1}{2n_n}\right) \tag{23}$$

The dilatancy process begins when the viscoplastic volumetric strain reaches the minimum plastic volumetric strain. The transition between compaction and dilatancy is very abrupt and depends on the confinement. $I_0$ and $I_u$ should properly define this change in order to follow the stress increment experimentally observed.

The following evolution rule is proposed for the dilatancy process

$$I_0(\kappa_v^{\text{vp}}) = I_0(\kappa_{v,\max}^{\text{vp}})\left[1 - \xi\sqrt{1 - \left(\frac{\kappa_v^{\text{vp}}}{\kappa_{v,\max}^{\text{vp}}}\right)^2}\right] \tag{24}$$

where $\xi = (p_{\max} - p_{\text{dilat}}/p_{\text{dilat}})$ represents the proportional difference between the maximum hydrostatic pressure $p_{\max}$ that can be reached in a triaxial test and the pressure for which dilatancy process begins $p_{\text{dilat}} = I_0(\kappa_{v,\max}^{\text{vp}})/3$. According to experimental results, this difference increases with confinement. Nevertheless, in practice, a constant mean value $\xi = 0.10$ can be considered.

During the dilatation process, the limit $I_u$ remains fix,

$$I_u(\kappa_v^{\text{vp}}) = I_u(\kappa_{v,\max}^{\text{vp}}) \tag{25}$$

### 4.7. Plastic potential function

The use of associated plastic flaw produces plastic dilatancy in high confinement regime in accordance with experimental results for concrete like materials under uniaxial tension and compression, and triaxial compression with low hydrostatic pressure. For higher pressures and depending on the loading path, this type of materials presents plastic compaction. This observation also matches the direction of the out ward normal of the yield surface. Nevertheless, in triaxial tests volumetric strains reaches a minimum depending on the confinement and then the dilatancy process begins. To consider this transition a non-associated flaw rule should be defined. According to Hartmann et al. [74], the direction of the plastic flaw in the deviatoric plane does not affect numerical results for high confinement pressures.

The plastic potential function is defined with the following expression that is identical to that used for the yielding surface:

$$G\left(\sigma_{ij};\kappa^{\text{vp}},\kappa_v^{\text{vp}}\right) = \frac{\frac{\sqrt{3J_2}}{G_{\text{cap}}(I_1,\kappa_v^{\text{vp}})} + \alpha I_1 + \beta\langle\sigma_{\max}\rangle - \gamma\langle-\sigma_{\max}\rangle + \frac{\delta(1-\alpha)}{K(\sigma_{ij},\kappa^{\text{vp}},\kappa_v^{\text{vp}})}I_1^2}{K(\sigma_{ij},\kappa^{\text{vp}},\kappa_v^{\text{vp}})(1-\alpha)(1+\delta)} - 1 = 0 \tag{26}$$

The only difference with the yielding surface is the definition of $G_{\text{cap}}$,

$$G_{\text{cap}}(I_1,\kappa_v^{\text{vp}}) = \begin{cases} 1 & I_1 \geq I_u^G(\kappa_v^{\text{vp}}) \\ 1 - \left(\dfrac{I_u^G(\kappa_v^{\text{vp}}) - I_1}{I_0^G(\kappa_v^{\text{vp}}) - I_u^G(\kappa_v^{\text{vp}})}\right)^2 & I_1 < I_u^G(\kappa_v^{\text{vp}}) \end{cases} \tag{27}$$

During the compaction process $I_u^G$ can be considered constant $I_u^G(\kappa_v^{\text{vp}}) = f_{c0}$ and $I_0^G(\kappa_v^{\text{vp}}) = I_0(\kappa_v^{\text{vp}})$. For dilatancy $I_u^G(\kappa_v^{\text{vp}}) = f_{c0}$ is also constant and $I_0^G(\kappa_v^{\text{vp}}) \rightarrow (-\infty)$, which is equivalent to the absence of the cap.

## 5. Application examples

### 5.1. Introduction

The proposed model has been implemented in a nonlinear dynamic 2D finite element program developed for research purposes.

As already mentioned, there are different hypothesis to explain the observed strength increase under increasing strain rate. Some authors [20–22] consider that this effect is a material property, while others attribute this effect to frictional effects [55], to inertial confinement [13,23] or to a combination of material viscosity and inertial effects [19].

Previous to the development of application examples, the viscoplastic parameters should be obtained from calibration with experimental results. For this purpose, numerical simulation of dynamic tension and compression tests under different strain rates are performed. The specimens are fixed at one end and different velocities are applied at the nodes on the other end.

Time integration is performed with Newmark method taking $\beta = 0.25$ and $\gamma = 0.50$.

The material properties used in the calibration of strain-rate dependence in tension correspond to a C55 concrete [85] and are presented in Table 1. Cylindrical elements of 40 mm diameter and 120 mm length are numerically analyzed using 32 axial symmetric finite elements with 4 nodes and 4 integration points. Different values of viscoplastic parameters and the resulting dynamic increments factors as a function of strain rates are compared with experimental values [85] in Fig. 11. Strain rate is calculated as defined in Ref. [85]. It can be observed that variation of the viscosity coefficient $\eta$ produces a vertical shift of the curve, while the variation of exponent N is responsible for the curve slope for high strain rates. From the calibration process it can be concluded that the values that best feet tension experimental DIF values are $\eta_t = 0.5$ s and $N_t = 2.0$.

For the case of uniaxial compression cylindrical elements of 51 mm diameter and length are modeled with 64 axial symmetric elements. Material properties correspond to concrete C40 in Ref. [86] and are presented in Table 1. The values $\eta_c = 0.0001$ y $N_c = 1$ are considered for the viscoplastic properties. The results are almost coincident with those obtained with an elastoplastic (rate independent) model. The numerical results obtained for the apparent compression dynamic increment factor corresponding to

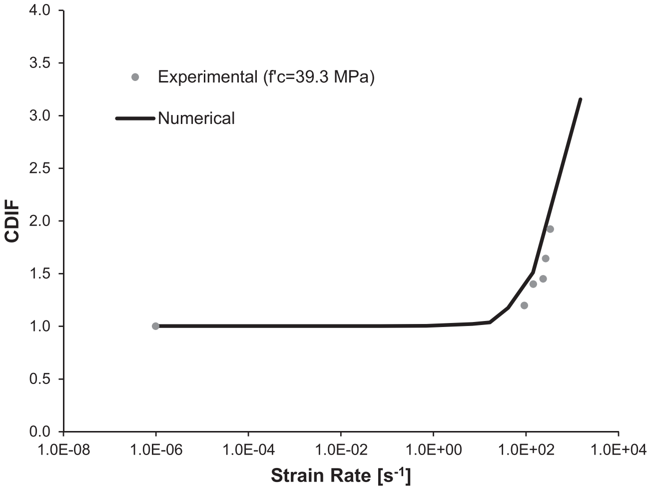

**Fig. 12.** CDIF. Compression viscoplastic parameters calibration. Experimental results by Tedesco et al. [86].

different strain rates are presented in Fig. 12, together with experimental results obtained for these specimens [86]. Strain rate in Fig. 12 is defined as described in Ref. [86], with the same definition used for tension tests. It should be observed that concrete strength seems to increase for strain rates greater than 10/s.

Nevertheless, it should be taken into account that non uniform multiaxial stress state takes place inside the specimens under dynamic uniaxial compression. This state includes confinement produced by inertial forces and frictional forces. As stated by Hao et al. [19], the strength measured in dynamic tests is not the dynamic uniaxial compression strength of concrete but a combination of concrete compression strength and structural behavior that is dependent on specimen dimensions.

The numerical results obtained with a very low viscosity value properly reproduce mean experimental results confirming that strain rate dependence in compression is mainly due to inertial effects and that the material itself is almost rate independent under uniaxial compression.

## 5.2. Quasistatic tests

### 5.2.1. Tension

The tension test performed by Hurlbut [87] on a cylindrical specimen of 108 mm diameter and 216 mm height is numerically reproduced using axial symmetric elements. The material properties used are presented in Table 1. Axial displacement increments are applied at one end of the specimen while the other end is fixed. The stress–strain curve obtained is presented and compared with experimental results in Fig. 13. It can be observed that the model accurately reproduces concrete behavior under quasistatic tension.

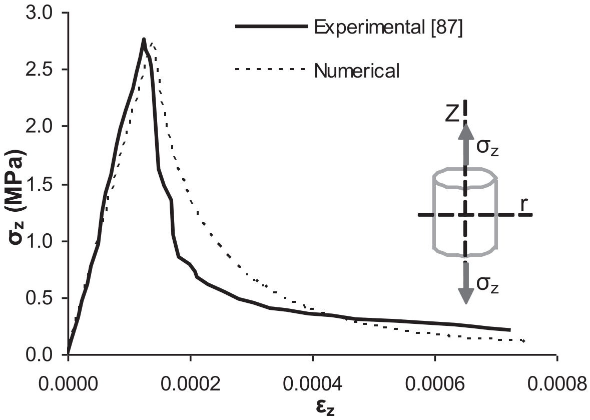

**Fig. 13.** Stress–strain curve for concrete under quasistatic tension. Comparison with experimental results [87].

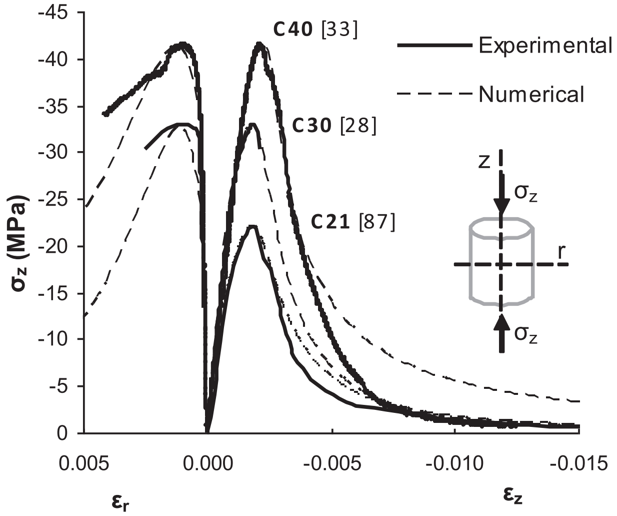

**Fig. 14.** Stress–strain curves for quasistatic uniaxial compression tests. Comparison with experimental results [28,33,87].

### 5.2.2. Uniaxial compression

The compression tests performed by different authors on different strength concretes [28,33,87] are numerically reproduced. In all cases cylindrical specimens were tested. The dimensions were: 108 mm diameter and 216 mm height [87]; 150 mm diameter and 300 mm height [28]; and 70 mm diameter and 140 mm height [33].

Only one quarter of the specimens is modeled with axial symmetric elements. Axial displacement increments are applied at one end of the specimen while the other end is fixed. The material properties are presented in Table 1. The stress–strain curves

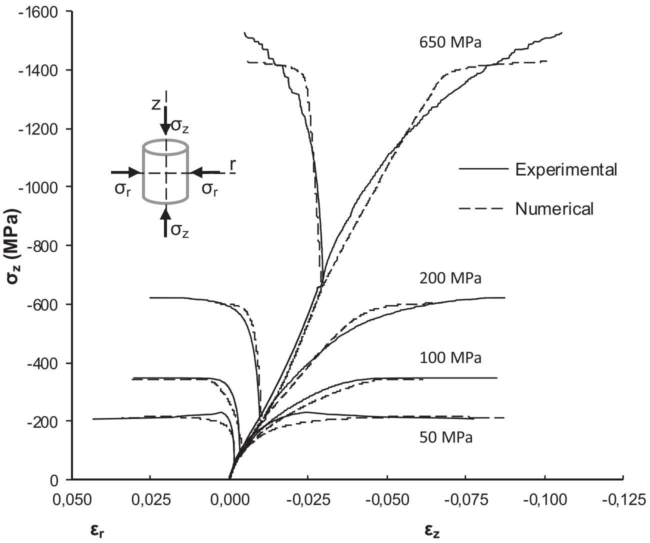

**Fig. 15.** Stress–strain curves for quasistatic triaxial compression tests of C40 concrete. Comparison with experimental results [33].

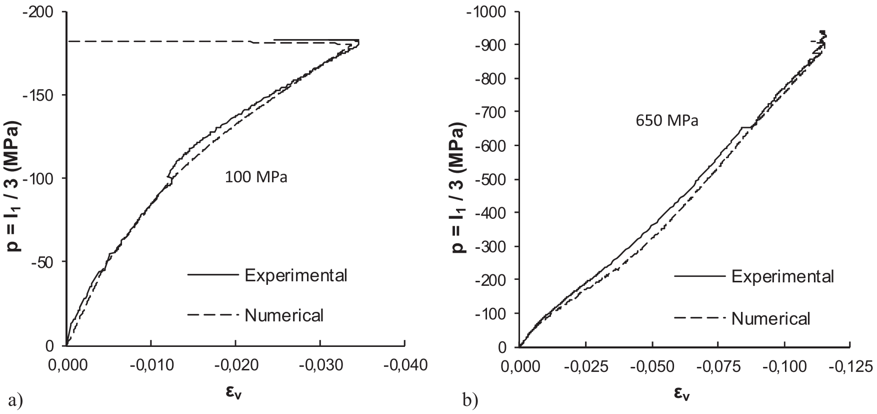

**Fig. 16.** Volumetric response for quasistatic triaxial compression tests with different confinement pressures. Comparison with experimental results [33]. a) Confinement pressure: 100 MPa; b) Confinement pressure: 650 MPa.

obtained for the different types of concrete are presented and compared with experimental results in Fig. 14.

### 5.2.3. *Triaxial compression*

The triaxial compression tests of cylindrical specimens of 70 mm diameter and 140 mm height under confinement pressure between 50 and 650 MPa [33,34] are simulated in this section. The load is applied in two stages: first hydrostatic pressure is increased up to a certain level of confinement and then, axial stress is increased controlling axial displacement and preserving the lateral stresses constant. Concrete properties are presented in Table 1.

Stress–strain curves in axial and radial directions numerically obtained are presented and compared with experimental results by Vu et al. [33] in Fig. 15. The numerical results for hydrostatic stage of the test with 650 MPa match experimental results since they were used for the definition of $I_0(\kappa_v^{\mathrm{vp}})$ (Eq. (22)). The volumetric responses are presented and compared with experimental results in Fig. 16.

The stress–strain curves numerically obtained are presented and compared with experimental results by Poinard et al. [34] in Fig. 17. The volumetric responses for different confinement pressures and their comparison with experimental results are presented in Fig. 18.

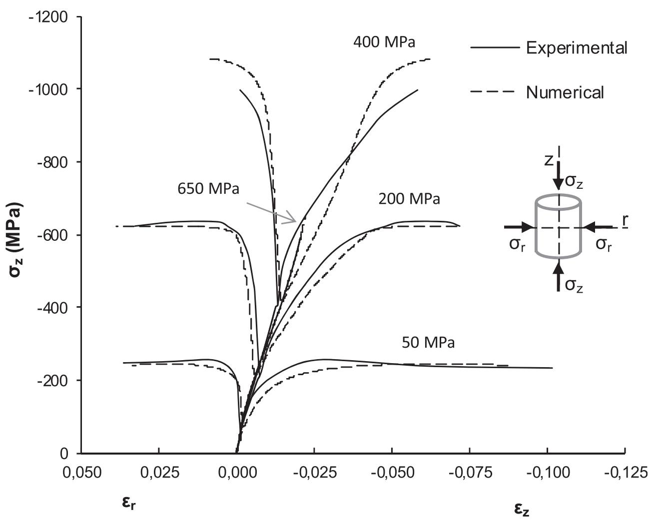

**Fig. 17.** Stress–strain curves for quasistatic triaxial compression tests of C40 concrete. Comparison with experimental results [34].

Volumetric strains decrease up to a minimum from which the dilatational process begins. The transition between these processes is very sharp and depends on the confinement level. During the dilatational process the material continues hardening until it reaches the peak strength value. It can be observed in Figs. 15 and 17 that the proposed model properly reproduces these effects for the analyzed cases.

### 5.2.4. *Hydrostatic compression and oedometric tests*

The hydrostatic and oedometric tests performed by Burlion et al. [35] on mortar specimens are numerically reproduced with the proposed model. The specimens are cylindrical with 50 mm diameter and 100 mm height. The material properties used for the mortar are presented in Table 1. Hydrostatic compression is applied through axial and radial pressure while for oedometric test only axial compression pressure is applied while lateral displacements are prevented.

It can be observed in Fig. 19 that numerical results properly reproduce experimental response. In the case of the oedometric test the stress are greater than those in the test. Nevertheless, the

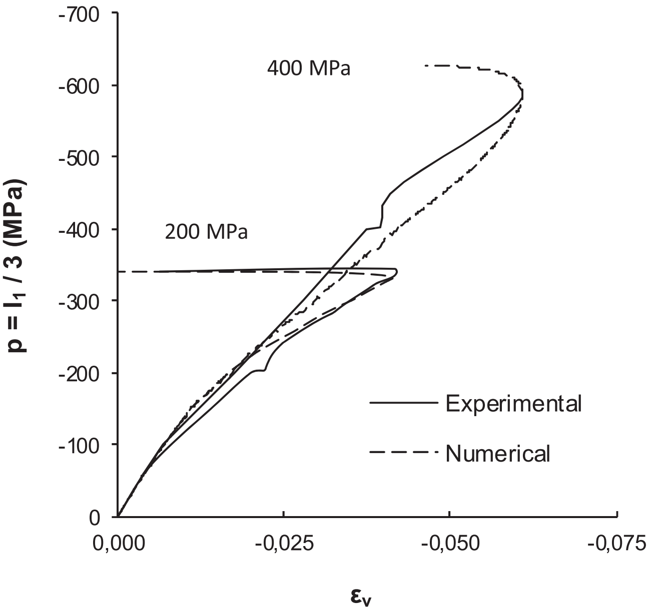

**Fig. 18.** Volumetric response for quasistatic triaxial compression tests with different confinement pressures. Comparison with experimental results [34].

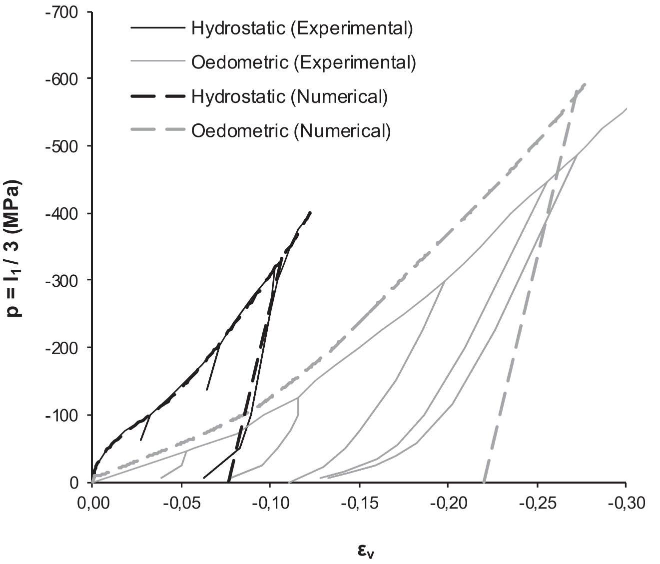

**Fig. 19.** Volumetric response in hydrostatic and oedometric tests of mortar. Comparison with experimental results [35].

numerical results presented in Fig. 19 confirm that the proposed model properly describes the coupling between volumetric and deviatoric response observed in frictional cohesive materials like concrete and mortar.

The hydrostatic and oedometric tests performed by Buzaud [88] and Gatuingt [89] respectively on high strength concrete (C70) are also numerically simulated. Concrete properties for both tests are presented in Table 1.

The volumetric responses obtained are presented and compared with experimental results in Fig. 20. Like in the case of mortar, the numerical results properly reproduce the observed experimental response for hydrostatic and oedometric tests. The responses are markedly different evidencing the coupling between deviatoric and hydrostatic components. A pronounced compaction process is observed in the case of the oedometric test due to the possibility of reorganization of the granular structure, while volumetric deformation are lower in the hydrostatic test since the granular structure is preserved preventing a greater compaction. Finally, it can be observed that compaction process is more pronounced for concrete case due to the heterogeneity of its granular structure.

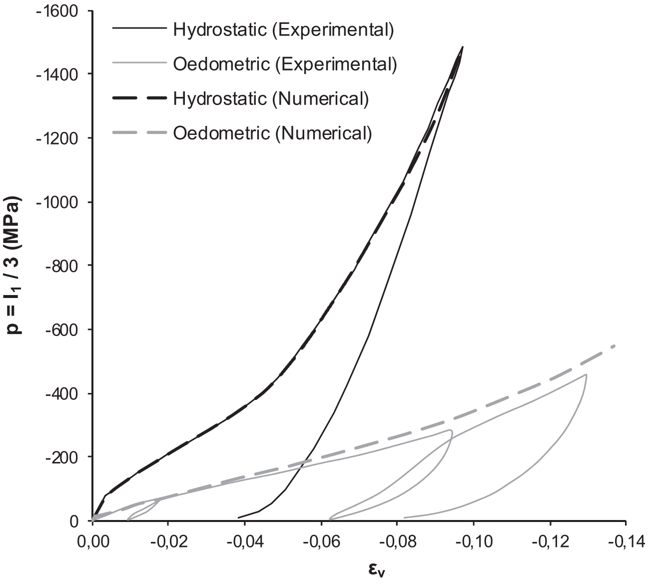

**Fig. 20.** Volumetric response in hydrostatic and oedometric tests of concrete. Comparison with experimental results by Buzaud [25] and Gatuingt [8] respectively.

**Table 2**
Specimens dimensions and applied strain rates.

| Test | $\dot{\varepsilon}$ s$^{-1}$ | Diam. *D* mm | Height *L* mm | Aspect ratio *L*/*D* |
|---|---|---|---|---|
| Grote et al. [12] | 290 | 11.9 | 11.7 | 0.98 |
| | 620 | 11.6 | 5.9 | 0.51 |
| | 1050 | 12 | 5.6 | 0.47 |
| | 1500 | 11.2 | 5.5 | 0.49 |
| Cazacu and Ross [8] | 52 | 76 | 76 | 1 |

### 5.3. *Dynamic tests*

#### 5.3.1. *Uniaxial compression*

The dynamic tests performed by Grote et al. [12] and Cazacu and Ross [89] on cylindrical concrete specimens are numerically simulated. The specimens dimensions and strain rates are presented in Table 2 while the material parameters for mortar and concrete identified as M46 and C70 respectively can be found in

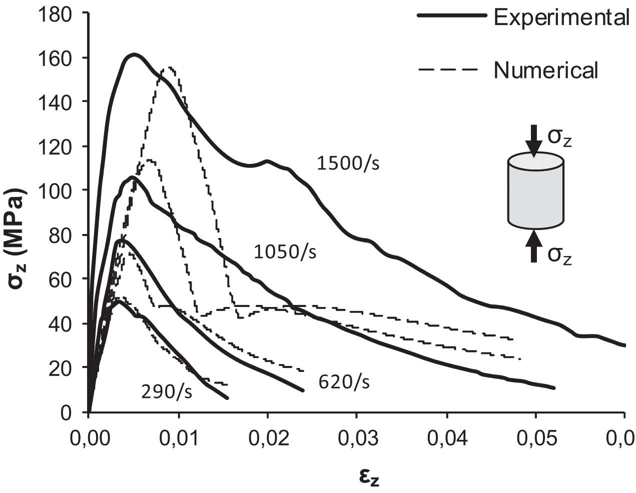

**Fig. 21.** Stress–strain curves for mortar under dynamic compression with different strain rates. Comparison with experimental results [12].

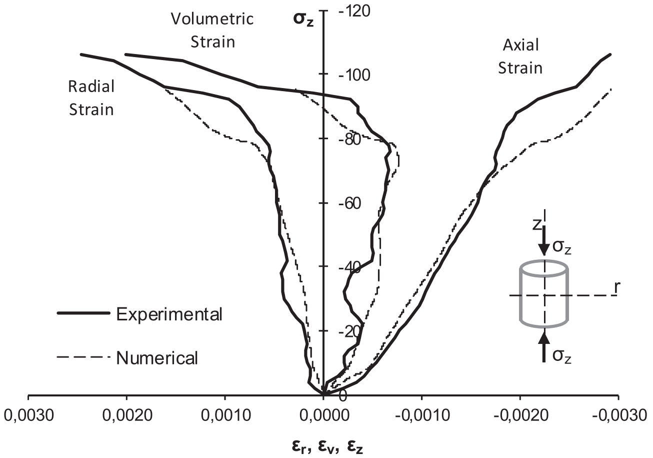

**Fig. 22.** Stress–strain curves for dynamic compression of concrete. Comparison with experimental results [89].

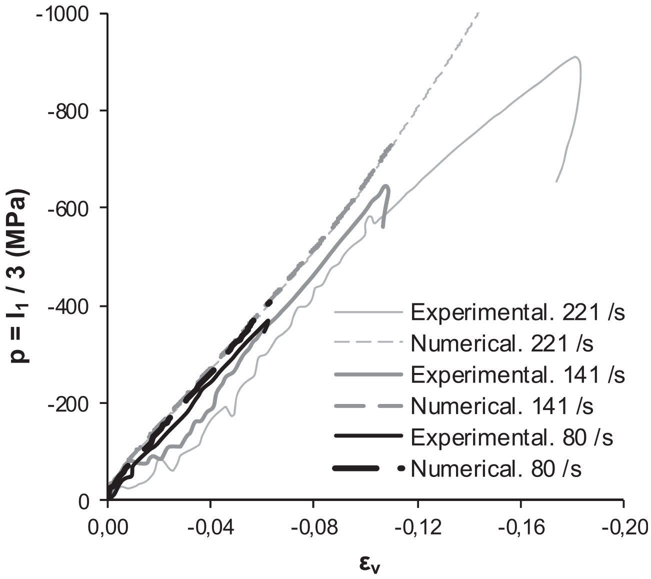

**Fig. 23.** Volumetric response for oedometric tests with different strain rates. Comparison with experimental results [25].

Table 1. The specimens are modeled with 128 axial symmetric elements in the case of $L/D = 1$ and 64 elements in the case of $L/D = 0.5$. The specimens are fixed at one end and different velocities are applied at the nodes on the other end to produce the strain rates indicated in Table 2.

The stress strain curves numerically obtained for the tests performed by Grote et al. [12] with different strain rates and their comparison with experimental results are presented in Fig. 21. Stress is calculated averaging the stress values on the specimen axis. It can be observed that the model is able to reproduce the strength increment due to increasing strain rate and the numerical stress–strain curves are close to experimental ones up to strain rates of the order of 1050/s. The elastic–viscoplastic model proposed is not able to reproduce the elastic modulus increase observed in experimental curves due to increasing strain rate. A viscoelastic approach is required to take into account this effect.

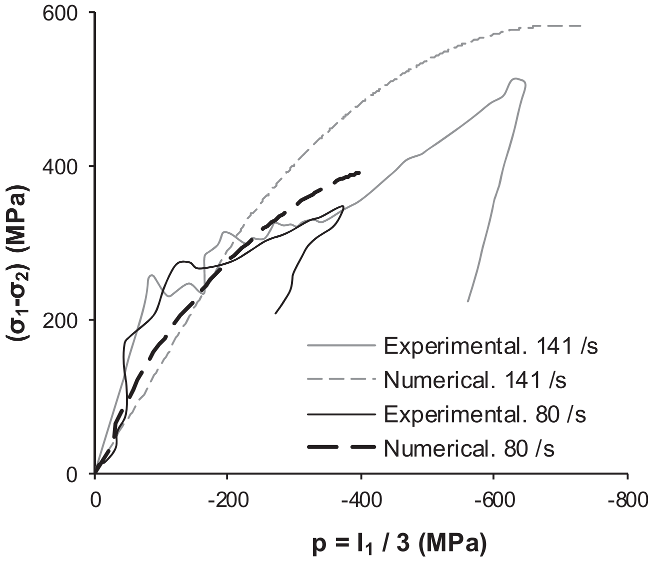

**Fig. 24.** Deviatoric stresses in oedometric tests under different strain rates. Comparison with experimental results [25].

The numerical results obtained for the tests performed by Cazacu and Ross [89] and their comparison with experimental results are presented in Fig. 22. It can be observed that numerically results not only adjust axial strains but also lateral and volumetric strains.

### 5.3.2. *Confined compression*

The compression tests performed by Forquin et al. [25] on cylindrical concrete specimens of 30 mm diameter and 40 mm height are numerically simulated. 32 axial symmetric elements are used to model the specimens. The material properties used for concrete are presented in Table 1. Axial velocities are applied at one end of the specimen, while axial displacements at the other end and radial displacement at the specimen's laterals are restrained. The tests corresponding to three different strains rates: 80/s; 141/s; and 221/s are reproduced.

The volumetric response numerically obtained for the different strain rates and the comparison with experimental results are presented in Fig. 23. It can be observed that the proposed model properly reproduces experimental curves up to a strain rate of 141/s. For greater strain rates the numerical curve departs from experimental results. The model tends to overestimate the stresses as in the case of quasistatic oedometric tests.

The deviatoric response numerically obtained and its comparison with experimental results is presented in Fig. 24. The stress differences numerically obtained are always greater than experimental values.

## 6. Conclusions

A constitutive model for concrete like materials that includes a “cap” on the hydrostatic axis, a new internal variable related to the compaction process, hardening rules that take into account the loading path and a plastic potential function that properly describes compaction to dilation transition is proposed in this paper.

The use of only one isotropic hardening variable based on plastic work is not enough to describe the behavior of concrete under non proportional loading including high confinement. For this reason, a new hardening variable that properly represents the stress evolution in these cases is included in the model. The use of non-associated plastic flaw is necessary to describe the transition between compaction and dilatational processes.

The developed model has been applied to different quasistatic and dynamic tests. As the strain rate is increased a finer mesh is needed to reproduce the dynamic response. Moreover, smaller time increments must be considered as the strain rate is increased and the time step for which results converge depends on the element size.

Both in tension and compression dynamical tests, the stress distribution in the specimen is not uniform. Particularly, for the case of compression the dynamic strength increment is mostly due to the inertial confinement and not to a material strain rate dependency. The effect of inertial confinement increases for decreasing aspects ratio $L/D$. The use of different viscoplastic parameters for tension and compression is appropriate to distinguish the material strain-rate dependency in tension.

The model is able to accurately reproduce the behavior of concrete under different quasistatic loading paths including hydrostatic pressures up to 16 times the compression strength. For the case of oedometric tests the model presents some tendency to overestimate the stresses as the materials compacts. The model properly reproduces compaction and dilatation processes.

The results obtained for hydrostatic and oedometric tests are markedly different evidencing the coupling between deviatoric and hydrostatic components. Also, the comparison between concrete and mortar results shows that compaction process is more pronounced for concrete due to the heterogeneity of its granular structure.

The model describes dynamic compression tests on concrete and mortar for different strain rates, properly reproducing not only the strength but also axial and transverse strains.

Finally, the model needs to be extended to take into account the elastic modulus increase observed in dynamic tests for high strain rates. This problem can be approached through a viscoelastic formulation.

## Acknowledgments

The financial support from CONICET (PIP 2011 -0105), CIUNT (26E/427) and National University of Tucumán is gratefully acknowledged. The authors also wish to thank Ms Amelia Campos for the English revision.

## References

[1] Crawford JE, Magallanes JM. The effects of modeling choices on the response of structural components to blast effects. Int J Prot Struct 2011;2(2):231–57.
[2] Coughlin AM, Musselman ES, Schokker AJ, Linzell DG. Behavior of portable fiber reinforced concrete vehicle barriers subject to blasts from contact charges. Int J Impact Eng 2010;37:521–9.
[3] Luccioni B, Luege M. Concrete pavement slab under blast loads. Int J Impact Eng 2006;32:1248–66.
[4] Schenker A, Anteby I, Gal E, Kivity Y, Nizri E, Sadot O. Full-scale field tests of concrete slabs subjected to blast loads. Int J Impact Eng 2008;35:184–98.
[5] Morales-Alonso G, Cendón DA, Gálvez F, Erice B, Sánchez-Gálvez V. Blast response analysis of reinforced concrete slabs: experimental procedure and numerical simulation. J Appl Mech 01/2011;78(5). http://dx.doi.org/10.1115/1.4004278.
[6] Nyström U, Gylltoft K. Numerical studies of the combined effects of blast and fragment loading. Int J Impact Eng 2009;36:995–1005.
[7] Lian YP, Zhang X, Zhou X, Ma ZTA. FEMP method and its application in modeling dynamic response of reinforced concrete subjected to impact loading. Comput. Methods Appl Mech Eng 2011;200:1659–70.
[8] Beppu M, Miwa K, Itohb M, Katayama M, Ohno T. Damage evaluation of concrete plates by high-velocity impact. Int J Impact Eng 2008;35:1419–26.
[9] Luccioni BM, Ambrosini RD, Danesi RF. Analysis of building collapse under blast loads. Eng Struct 2004;26:63–71.
[10] Kwasniewski L. Nonlinear dynamic simulations of progressive collapse for a multistory building. Eng Struct 2010;32:1223–35.
[11] Shi Y, Li Z-X, Hao H. A new method for progressive collapse analysis of RC frames under blast loading. Eng Struct 2010;32:1691–703.
[12] Grote DL, Park SW, Zhou M. Dynamic behavior of concrete at high strain rates and pressures: I. Experimental characterization. Int J Impact Eng 2001;25:869–86.
[13] Cotsovos DM, Pavlovic MN. Numerical investigation of concrete subjected to high rates of uniaxial tensile loading. Int J Impact Eng 2008;35:319–35.
[14] Zhang M, Wu HJ, Li QM, Huang FL. Further investigation on the dynamic compressive strength enhancement of concrete-like materials based on split Hopkinson pressure bar tests. Part I: experiments. Int J Impact Eng 2009;36:1327–34.
[15] Erzar B, Forquin P. An experimental method to determine the tensile strength of concrete at high rates of strain. Exp Mech 2010;50(7):941–55.
[16] Mazars J, Millard A. Dynamic behavior of concrete and seismic engineering. ISTE-WILEY; 2010.
[17] CEB-FIP Model Code 1990. Comité Euro-International du Béton. Trowbridge, Wiltshire, UK: Redwood Books; 1990. p.48–51.
[18] Ngo T, Mendis P. Modelling the dynamic response and failure modes of reinforced concrete structures subjected to blast and impact loading. Struct Eng Mech 2009;32(2):269–82.
[19] Hao Y, Hao H, Li Z-X. Numerical analysis of lateral inertial confinement effects on impact test of concrete compressive material properties. Int J Prot Struct 2010;1(1):145–68.
[20] Sercombe J, Ulm F-J, Toutlemonde F. Viscous hardening plasticity for concrete in high rate dynamics. J Eng Mech ASCE 1998;124(9):1050–7.
[21] Weerheijm J, Van Doormaal JCAM. Tensile failure of concrete at high loading rates: new test data on strength and fracture energy from instrumented spalling tests. Int J Impact Eng 2007;34:609–26.
[22] Ruiz G, Zhang XX, Tarifa M, Yu R, Camara M. Fracture energy of high-strength concrete under different loading rates. An Mecánica Fract 26 2009;2:513–8.
[23] Schwer L. Strain rate induced strength enhancement in concrete: much ado about nothing?. In: 7th European LS-DYNA Users Conference, Salzburg, Austria, May 14–15, 2009; 1–17.
[24] Shkolnik IE. Influence of high strain rates on stress–strain relationship, strength and elastic modulus of concrete. Cem Concr Compos 2008;30:1000–12.
[25] Forquin P, Gary G, Gatuingt F. A testing technique for concrete under confinement at highrates of strain. Int J Impact Eng 2008;35:425–46.
[26] Hao Y, Hao H. Numerical evaluation of the influence of aggregates on concrete compressive strength at high strain rate. Int J Prot Struct 2011;2(2):177–206.
[27] Dupray F, Malecot Y, Daudeville L, Buzaud E. A mesoscopic model for the behaviour of concrete under high confinement. Int J Numer Anal Meth Geomech 2009;33:1407–23.
[28] Sfer D, Carol I, Gettu R, Etse G. Experimental study of the triaxial behaviour of concrete. J Eng Mech ASCE 2002;128(2):156–63.
[29] Lu X, Hsu C. Behavior of high strength concrete with and without steel fiber reinforcement in triaxial compression. Cem Concr Res 2006;36:1679–85.
[30] Bohwan O, Myung-Ho L, Sang-John P. Experimental study of 60 MPa concrete under triaxial stress. Bangalore: India: Structural Engineers World Congress; 2007, 1–12.
[31] Gabet T, Malecot Y, Daudeville L. Ultimate strength of plain concrete under extreme combined stresses: triaxial and proportional stress paths. Rev Eur Génie Civ 2006;10(3):375–90.
[32] Gabet T, Malecot Y, Daudeville L. Triaxial behaviour of concrete under high stresses: influence of the loading path on compaction and limit status. Cem Concr Res 2008;38(3):403–12.
[33] Vu XH, Malecot Y, Daudeville L, Buzaud E. Experimental analysis of concrete behavior under high confinement: effect of the saturation ratio. Int J Solids Struct 2009;46:1105–20.
[34] Poinard C, Malecot Y, Daudeville L. Damage of concrete in a very high stress state: experimental investigation. Mater Struct 2010;43:15–29.
[35] Burlion N, Pijaudier-Cabot G, Dahan N. Experimental analysis of compaction of concrete and mortar. Int J Numer Anal Methods Geomech 2001;25:1467–86.
[36] Burlion N, Gatuingt F, Pijaudier-Cabot G, Daudeville L. Compaction and tensile damage in concrete: constitutive modelling and application to dynamics. Comput. Methods Appl Mech Eng 2000;183:291–308.
[37] Luege M, Luccioni B, Danesi R. Modelo de daño dependiente de la velocidad de deformación. Rev Int Mét Num Cálculo Diseño Ing 2002;18(2):411–31.
[38] Luccioni B, Rougier V. A plastic damage approach for confined concrete. Comput Struct 2005;83:2238–56.
[39] González JM, Miquel Canet J, Oller S, Miró R. A viscoplastic constitutive model with strain rate variables for asphalt mixtures-numerical simulation. Comput Mater Sci 2007;38:543–60.
[40] Ning JG, Liu HF, Shang L. Dynamic mechanical behavior and the constitutive model of concrete subjected to impact loadings. Sci China Ser G Phys Mech Astron 2008;51(11):1745–60.
[41] Pedersen RR, Simone A, Sluys LJ. An analysis of dynamic fracture in concrete with a continuum visco-elastic visco-plastic damage model. Eng Fract Mech 2008;75:3782–805.
[42] Rabczuk T, Eibl J. Simulation of high velocity concrete fragmentation using SPH-MLSPH. Int J Numer Methods Eng 2003;56:1421–44.
[43] Jankowiak T, Lodygowski T. Using of smoothed particle hydrodynamics (sph) method for concrete application. In: CMM-2011 Computer Methods in Mechanics, 9 -12 May 2011, Warsaw, Poland; 2011; 1–2.
[44] Cusatis G, Bazant ZP, Cedolin L. Confinement-shear lattice model for concrete damage in tension and compression: I. Theory. J Eng Mech 2003;129(12):1439–48.
[45] Cusatis G, Bazant ZP, Cedolin L. Confinement-shear lattice model for concrete damage in tension and compression: II. Computation and validation. J Eng Mech 2003;129(12):1449–58.
[46] Hentz S, Donzé FV, Daudeville L. Discrete element modelling of concrete submitted to dynamic loading at high strain rates. Comput Struct 2004;82:2509–24.
[47] Tavarez FA, Plesha ME. Discrete element method for modelling solid and particulate materials. Int J Numer Methods Eng 2007;70:379–404.
[48] Lu Y. Modelling of concrete structures subjected to shock and blast loading: an overview and some recent studies. Struct Eng Mech 2009;32(2):235–49.
[49] Riedel W, Wicklein M, Thoma K. Shock properties of conventional and high strength concrete: experimental and mesomechanical analysis. Int J Impact Eng 2008;35:155–71.
[50] Tu Z, Lu Y. Evaluation of typical concrete material models used in hydrocodes for high dynamic response simulations. Int J Impact Eng 2009;36:132–46.
[51] Tu Z, Lu Y. Mesoscale modelling of concrete for static and dynamic response analysis part 1: model development and implementation. Struct Eng Mech 2011;37(2):197–213.
[52] William EM, Akers SE, Reed PA. Laboratory characterization of fine aggregate cementitious material. Report N° ERDC/GSL TR-05-16, Geotechnical and Structures Laboratory, U.S. Army Engineer Research and Development Center, 3909 Halls Ferry Road, Vicksburg, MS 39180-6199. 2005;1–102.
[53] Bischoff P, Perry S. Compressive behaviour of concrete at high strain rates. Mater Struct 1991;24:425–50.
[54] Erzar B, Forquin P, Pontiroli C, Buzaud E. Influence of aggregate size and free water on the dynamic behaviour of concrete subjected to impact loading. In: International Conference on Experimental Mechanics, Poitiers, France, July 4–9, 2010; EPJ Web of Conferences 6, 39007, EDP Sciences, 2010; 1–8.
[55] Mu ZC, Dancygier AN, Zhang W, Yankelevsky DZ. Revisiting the dynamic compressive behavior of concrete-like materials. Int J Impact Eng 2012;49:91–102.

[56] Xu K, Lu Y. Numerical simulation study of spallation in reinforced concrete plates subjected to blast loading. Comput Struct 2006;84:431–8.
[57] Desai C, Siridwardane H. Constitutive laws for engineering materials, with emphasis on geologic materials. Prentice Hall, Inc., Englewood Cliffs, New Jersey, 1984; 83–203.
[58] Rots J. Strain softening analysis of concrete fracture specimens. In: Wittmann FH, editor. Fracture toughness and fracture energy of concrete; Elsevier Amsterdam; 1986: 137–148.
[59] Lubliner L, Oliver J, Oller S, Oñate E. A plastic damage model for concrete. Int J Solids Struct 1989;25(3):299–326.
[60] Luccioni B, Oller S. A directional damage model. Comput Methods Appl Mech Eng 2003;192:1119–45.
[61] Perzyna P. Fundamental problems in viscoplasticity. Adv Appl Mech 1966;9: 244–368.
[62] Lu Y, Song Z, Tu Z. Analysis of dynamic response of concrete using a mesoscale model incorporating 3D effects. Int J Prot Struct 2010;1(2):197–217.
[63] Gebbeken N, Hartmann TA. New methodology for the assessment of the EoS data of concrete. Int J Prot Struct 2010;1(3):299–317.
[64] Bazant Z, Prat P. Microplane model for brittle plastic materials. ASCE-EM 1988;114:1672–702.
[65] Pierard O, Llorca J, Segurado J, Doghri I. Micromechanics of particle-reinforced elasto–viscoplastic composites: finite element simulations versus affine homogenization. Int J Plast 2007;23:1041–60.
[66] Abou-Chakra Guéry A, Cormery F, Su K, Shao JF, Kondo D. A micromechanical model for the elasto–viscoplastic and damage behavior of a cohesive geomaterial. Phys Chem Earth 2008;33:416–21.
[67] Johnson GR, Holmquist TJ. An improved constitutive model for brittle materials. AIP Conf Proc 1994;309:981.
[68] Malvar LJ, Crawford JE, Wesevich JW. A plasticity concrete material model for Dyna3D. Int J Impact Eng 1997;19(9–10):847–73.
[69] Magallanes J, Wu Y, Malvar L. and Crawford J. Recent improvements to release III of the K&C Concrete Model. In: 11th International LS-DYNA Users Conference, Detroit, USA , 2010; 1(3):37–48.
[70] Noble C, Kokko E, Darnell I, Dunn T, Hagler L, Leininger L. Concrete model descriptions and summary of benchmark studies for blast effects simulations. Technical Report UCRL-TR-215024, U.S Dep. of Energy & Lawrence Livermore National Laboratory, Livermore, California, USA, 2005; 1–28.
[71] Gebbeken N, Ruppert M. A new material model for concrete in high-dynamic hydrocode simulations. Arch Appl Mech 2000;70:463–78.
[72] Riedel W, Thoma K, Hiermaier S. Numerical analysis using a new macroscopic concrete model for hydrocodes. In: SKA, editor. Proc. 9th int. symposium on interaction of effects of munitions with structures, Berlin-Strausberg, Germany; 1999. p. 315–22.
[73] Tu Z, Lu Y. Modifications of RHT material model for improved numerical simulation of dynamic response of concrete. Int J Impact Eng 2010;37: 1072–82.
[74] Hartmann T, Pietzsch A, Gebbeken N. A hydrocode material model for concrete. Int J Prot Struct 2010;1(4):443–68.
[75] Willam KJ, Warnke EP. Constitutive model for the triaxial behavior of concrete. Int Assoc Bridge Struct Eng 1975;7519:1–31.
[76] Zhou XQ, Hao H. Mesoscale modelling and analysis of damage and fragmentation of concrete slab under contact detonation. Int J Impact Eng 2009;36: 1315–26.
[77] Zhou XQ, Hao H. Mesoscale modelling of concrete tensile failure mechanism at high strain rates. Comput Struct 2008;86:2013.
[78] Folino P, Etse G, Will A. Performance dependent failure criterion for normal and high-strength concretes. J Eng Mech 2009;135(12):1393–409.
[79] Lubliner J. Plasticity theory. New York: MacMillan Publishing; 1990, p.55-67.
[80] Aráoz GF, Luccioni BM. Modelación del hormigón en régimen de alto confinamiento. In: AMCA, editor. Mecánica Computacional. Electronic Publication; 2011. XXX(8): 571–95.
[81] Le Nard H, Bailly P. Dynamic behaviour of concrete: the structural effects on compressive strength increase. Mech Cohes-Frict Mater 2000;5:491–510.
[82] Simo JC, Hughes TJR. Computational inelasticity. New York: vol. 7: Interdisciplinary Applied Mathematics, Springer; 1998. 105–112.
[83] Luccioni B, Oller S, Danesi R. Coupled plastic damage model. Comput Methods Appl Mech Eng 1996;129:81–9.
[84] Aráoz GF, Luccioni BM. Modelo viscoplástico para materiales cohesivo-friccionales. In: AMCA, editor. Mecánica Computacional. Electronic Publication; 2009; XXVIII(11): 877–99.
[85] Brara A, Klepaczko JR. Experimental characterization of concrete in dynamic tension. Mech Mater 2006;38:253–67.
[86] Tedesco JW, Powell JC, Allen Ross C, Hughes ML. A strain-rate-dependent concrete material model for ADINA. Comput Struct 1997;64(5–6):1053–67.
[87] Hurlbut B. Experimental and computational investigation of strain-softening in concrete [Master's thesis]. USA: University of Colorado, Boulder; 1985; p.1–256.
[88] Gatuingt F. Prévision de la rupture des ouvrages en béton sollicités en dynamique rapide [Thése de doctorat de]. Cachan, France: l'ENS de Cachan; 1999. 83–118.
[89] Cazacu O, Ross CA. Experimental and theoretical investigation of concrete high-strain rate behavior. In: Proceedings of the 2003 Society of Experimental Mechanics Annual Conference and Exposition on Experimental and Applied Mechanics, June 2-4 2003. North Carolina, USA: Charlotte; 2003. 1–7.